Progress In Electromagnetics Research, Vol. 122, 467–496, 2012

AXIAL-FLUX PERMANENT-MAGNET MOTOR DESIGN FOR ELECTRIC VEHICLE DIRECT DRIVE USING SIZING EQUATION AND FINITE ELEMENT ANALYSIS

A. Mahmoudi*, N. A. Rahim, and H. W. Ping

UMPEDAC, Engineering Tower, University of Malaya, Kuala Lumpur, Malaysia

Abstract—The design process of a double-sided slotted TORUS axial-flux permanent-magnet (AFPM) motor suitable for direct drive of electric vehicle (EV) is presented. It used sizing equation and Finite Element Analysis (FEA). AFPM motor is a high-torque-density motor easily mounted compactly onto a vehicle wheel, fitting the wheel rim perfectly. A preliminary design is a double-sided slotted AFPM motor with 6 rotor poles for high torque-density and stable rotation. In determining the design requirements, a simple vehicle-dynamics model that evaluates vehicle performance through the typical cruising trip of an automobile was considered. To obtain, with the highest possible torque, the initial design parameters of the motor, AFPM's fundamental theory and sizing equation were applied. Vector Field Opera-3D 14.0 commercial software ran the FEA of the motor design, evaluating and enhancing accuracy of the design parameters. Results of the FEA simulation were compared with those obtained from the sizing equation; at no-load condition, the flux density at every part of the motor agreed. The motor's design meets all the requirements and limits of EV, and fits the shape and size of a classical-vehicle wheel rim. The design process is comprehensive and can be used for an arbitrary EV with an arbitrary cruising scenario.

1. INTRODUCTION

Protection of natural environments sparked interest in electric vehicle (EV), a non-polluting personal transport. EV first appeared in 1870 but was for many years not further developed.The past 10 years, however, have seen developmental progress of EV [1]. Battery, electric

Received 4 September 2011, Accepted 22 November 2011, Scheduled 8 December 2011
* Corresponding author: Amin Mahmoudi (amaminmahmoudi@gmail.com).

motor, motor drive circuit, and transmission gears make up EV's power system. Researchers and designers look into increasing the efficiency and reliability of EV power systems. Improvement of each subsystem increases the overall efficiency, and consequently, the driving range. One reason for EV's little commercial success over the past century is that its efficiency had yet to reach the public's expectations for it [2]. Low price and simple but strong physical structure are the reasons for induction motor's wide application in EV [3]. Also, it can withstand high overloading and have low torque ripple. Its disadvantages, however, are low power-density, huge size and average efficiency. Permanent-magnet motor competing with induction motor in EV application has recently been developed; it fulfills the required high efficiency, small size, and high power density [4–7]. A motor designed for EV can be classified as direct drive or indirect drive [8, 9]. Direct drive excludes transmission gears and mechanical differential including the associated energy losses.The motor is mounted inside vehicle wheel rim and turns the wheel directly, so it must be compact and have high torque [10].

Permanent-magnet machines generally can be axial-flux or radial-flux [11]. Advantages of axial-flux permanent-magnet (AFPM) motors over conventional radial-flux permanent-magnet (RFPM) motors include high torque-to-weight ratio, good efficiency, adjustable air-gap, balanced rotor-stator attractive forces, and better heat-removal [12–14]. They can be easily and compactly mounted onto vehicle wheel, fitting the wheel rim perfectly, suitable for direct drive applications. AFPM machines can be single-sided or double-sided, with or without armature slots, with or without armature core, with internal or external permanent-magnet rotors, with surface-mounted or interior permanent-magnet, and single-stage or multistage machines [15]. Double-sided configurations have either external stator or external rotor. An external stator means fewer permanent magnets but poor use of winding, whereas an external rotor is considered particularly advantageous to machine topology. Topologies for double-sided AFPM machines are one-stator-two-rotor (TORUS) and two-stator-one-rotor (AFIR) [16]. Among various configurations, slotted TORUS AFPM is the most applicable [17]; double-sided slotted TORUS AFPM configuration thus is the subject of this paper, as is its design for EV application.

Huang et al. derived the general-sizing and power-density equations for RFP machines, also a systematic method for comparing the capabilities of machines of various topologies [18]. In 1999, they developed the sizing equation for AFPM machines [19]. Aydin et al. presented optimum-sized AFPM machines for TORUS and

AFIR topologies [20, 21]. Since then, there have been only a few papers reporting application of sizing equation to AFPM machine design, no doubt because of its limits (e.g., magnet skewing and winding configurations cannot be considered) [22]. Unlike traditional RFPM machines, AFPM machines have a unique construction, including a complex magnetic circuit that usually needs 3D Finite Element Analysis (FEA) for design of the machines. FEA, though accurate, has a long computation time that still can increase with the remodeling (including re-meshing) required when machine geometry changes. A solution to this problem is the application of 3D FEA complementarily to sizing equation. The electromagnetic torque against diameter ratio is extracted from AFPM machine's fundamental equation, to obtain maximum torque. A sizing equation capable of calculating,with acceptable accuracy and speed, flux distribution and torque characteristics, is then applied to obtain the initial AFPM motor dimensions, before FEA is applied, for permanent-magnet skewing, accuracy enhancing, and the desired electric motor parameters.

This research aims for an electric motor that is suitable for electric vehicle application. The limits of the sizing equation used in the design was overcome by FEA, which increased accuracy, so the resulting motor has high power density, a most-sinusoidal back-EMF waveform, and reduced torque.

The paper is organized as follows: Section 2 presents the basic equations for vehicle dynamics; Section 3 extracts the sizing equations that give the TORUS AFPM machine its power-producing potential; Section 4 presents the electromagnetic field analysis via FEA on the proposed motor topology, from the sizing equation, for the desired parameters, results of the FEA simulation results and of the sizing equation compared; Section 5 concludes with discussing the results.

2. VEHICLE DYNAMIC, DESIGN RESTRICTIONS AND REQUIREMENTS

A simple model of vehicle dynamics that evaluates vehicle performance is herewith presented. A simplified vehicle driving resistance force or road load (F_{rm}) consists of rolling resistance force (f_{ro}), climbing resistance force (f_{st}), and aerodynamic drag force (f_l):

$$F_{rm} = f_{ro} + f_{st} + f_l \tag{1}$$

Rolling resistance force (f_{ro}) is caused by on-road tire deformation:

$$f_{ro} = f_r \cdot M \cdot a_g \tag{2}$$

where f_r, M, and a_g are rolling resistance coefficient, vehicle mass, and gravity acceleration, respectively. Climbing resistance (f_{st} with positive operational sign) and downward force (f_{st} with negative operational sign) are given by:

$$f_{st} = M \cdot a_g \cdot \sin\alpha \tag{3}$$

where α is angle of vehicle movement relative to horizon. Aerodynamic drag force (f_l) is air viscous resistance on vehicle:

$$f_l = \frac{1}{2}\rho_a \cdot C_d \cdot S \cdot (v + v_0)^2 \tag{4}$$

where ρ_a is air density, C_d is air-resistance coefficient, S is frontal projected area, v is vehicle speed, and v_0 is headwind speed. Acting as propulsion, driving force is applied to wheels to overcome driving resistance. Driving force lower than driving resistance does not make vehicle roll. In angular movement, minimum required torque for vehicle propulsion is:

$$\tau_{\min} = r \times F_{rm} \tag{5}$$

where r is position vector. Minimum power required is thus:

$$P_{\min} = \tau_{\min} \cdot \omega_m \tag{6}$$

where ω_m is angular speed.The energy required for acceleration (a), too, must factor in calculations of the vehicle movement. The power required to accelerate the EV is:

$$P_{accel} = M \cdot v \cdot a \tag{7}$$

The power required in total is:

$$P_{out} = P_{accel} + P_{\min} \tag{8}$$

In designing the motor propulsion, the vehicle dynamics should first be determined. Fig. 1 is an EV cruising scenario that includes the EV's typical-trip elements such as increased speed, constant speed, and braking action. Power needed by the vehicle is calculated from the proposed driving cycle in Fig. 1, together with Equations (1) to (8). Note that in this study, 4 motors were needed, mounted onto the vehicle wheels to provide the required power. Table 1 lists the parameters of the study.

The design of an AFPM motor appropriate for an electric vehicle should consider both requirements and limits. Some of the motor's parameters and characteristics cannot vary much,the inability either inherent or owing to material and/or application limits. Table 2 lists the limits of the design procedure.

3. THE AXIAL-FLUX PERMANENT-MAGNET MOTOR DESIGN PARAMETERS

3.1. The Fundamental Design Equations

The air-gap flux density (B_g) is calculated by using remanence flux density (B_r) and the relative permeability (μ_{ra}) of the permanent magnet, also the geometrical dimensions of the air-gap, and the permanent magnet geometry as in [15]:

$$B_g = k_{\sigma pm} \frac{B_r}{1 + \mu_{ra} \frac{k_C g}{L_{pm}} \frac{S_{pm}}{S_g}} \tag{9}$$

where, g and L_{pm} are respectively the air-gap thickness and permanent magnet thickness; S_g and S_{pm} are respectively the air-gap area and

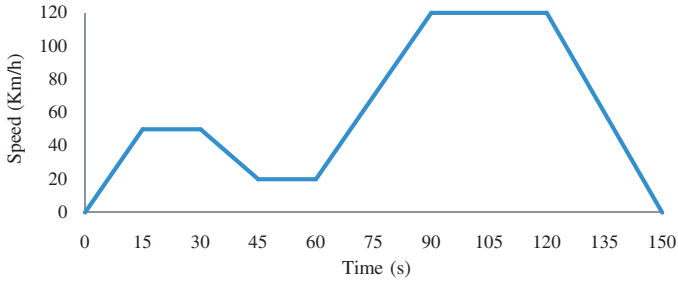

Figure 1. Proposed driving cycles for electric-vehicle design.

Table 1. Parameters used in this study.

Vehicle Specification	
Weight of Vehicle	80 kg
Weight of Passengers	4×70 kg
Wheel Diameter	0.35 m
Tire Set	4 units
Rim Diameter	14 inch
Drive System	direct-drive
Frontal Area (S)	2.5 m^2
Air Resistance Coefficient (C_d)	0.35
Tire Resistance Coefficient (f_r)	2.5×10^{-3}
Air Density (ρ_a)	1.22 kg/m^3
Maximum Speed (v_{max})	120 km/h

Table 2. Design restrictions and requirements.

Dimensional Constrains	
Stator Outer Diameter	$\leq 350\,\text{mm}$
Total Axial-Length	$\leq 100\,\text{mm}$
Material Limitations	
Permanent Remanence	1.3 T
Stator and Rotor Core Flux Density	$B_{cs}, B_{cr} \leq B_{\max} = 1.5$ T
Limitations on Power System	
Rated line-to-line Voltage	$\leq 150\,\text{V}$
Requirements	
Minimum Torque	33 Nm
Output Power	10 kW
Motor Efficiency	$\geq 90\%$

permanent magnet area. $k_{\sigma PM}$ is a factor that takes into account the leakage flux and k_C>1 is the Carter coefficient. The air-gap magnetic flux density in fact reduces under each slot opening, owing to decreased magnetic permeance. The Carter coefficient considers this change in magnetic flux density (caused by slot opening) by defining a fictitious air-gap greater than the physical one, and is computed from [15]:

$$k_C = \frac{t}{t - \gamma g} \tag{10}$$

where t is the average slot pitch, and the fictitious air-gap coefficient γ is defined by:

$$\gamma = \frac{4}{\pi}\left[\frac{W_s}{2g}\tan^{-1}\left(\frac{W_s}{2g}\right) - \ln\sqrt{1+\left(\frac{W_s}{2g}\right)^2}\right] \tag{11}$$

where W_s is the width of the slot opening. Fig. 2 is construction of the double-sided slotted AFPM machine including its configurations for rotor, stator, and slot. Assuming a sinusoidal waveform for the air-gap flux density, the average electromagnetic torque τ of a double-sided AFPM motor is calculated from:

$$\tau = \frac{\pi}{4} B_g A_{lin}\, D_o^3\, \lambda(1-\lambda^2) \tag{12}$$

where A_{lin} is the linear current density of the machine's inner radius and λ is AFPM diameter ratio $D_i\,/D_o$; D_o is diameter of the machine's outer surface; D_i is diameter of the machine's inner surface. For a given outer diameter and magnetic and electrical loading, AFPM

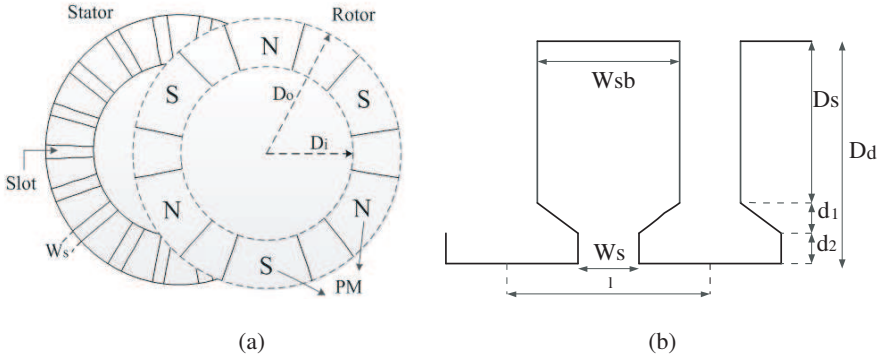

Figure 2. Double-sided axial-flux permanent-magnet construction. (a) Stator and rotor of the AFPM machine configuration. (b) Internal stator slot configuration.

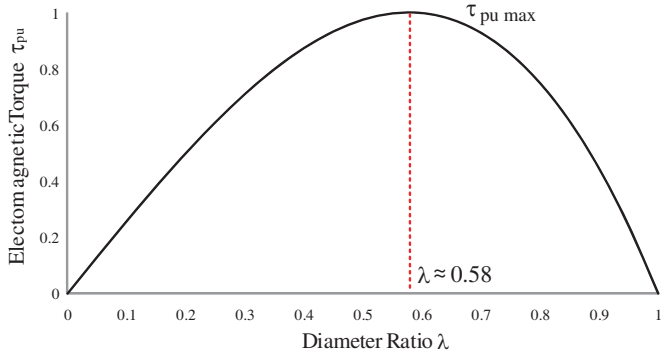

Figure 3. Per-unit electromagnetic torque τ_{pu} against diameter ratio λ.

machine's diameter ration λ is very important as it determines the motor's maximum torque. Fig. 3 shows the per-unit electromagnetic torque against the diameter ratio. The maximum torque is achievable when $\lambda \approx 0.58$.

3.2. The Sizing Equation

The main dimensions of each electrical machine are determined via electrical-machine-output power equation. Assuming negligible leakage inductance and resistance, the rated power is expressed as [19]:

$$P_{out} = \eta \frac{m}{T} \int_0^T e\,(t) \cdot i\,(t)\,dt = m\,k_p\,\eta E_{pk} I_{pk} \tag{13}$$

$e(t)$ is phase air-gap EMF, $i(t)$ is phase current, η is machine efficiency, m is the number of machine phases, and T is the period of one EMF cycle; E_{pk} and I_{pk} respectively are peaks of phase air-gap EMF and of current; k_p is electrical power waveform factor, defined as:

$$K_p = \frac{1}{T}\int_0^T \frac{e(t)\cdot i(t)}{E_{pk}\cdot I_{pk}}dt = \frac{1}{T}\int_0^T f_e(t)\cdot f_i(t)dt \tag{14}$$

where $f_e(t) = e(t)/E_{pk}$ and $f_i(t) = i(t)/I_{pk}$ are expressions for normalized EMF and current waveforms. For effect of current, the current waveform factor (k_i) is defined as:

$$k_i = \frac{I_{pk}}{I_{rms}} = \frac{1}{\sqrt{\frac{1}{T}\int_0^T \left(\frac{i(t)}{I_{pk}}\right)^2 dt}} \tag{15}$$

where I_{rms} is phase-current rms value. Table 3 lists typical waveforms and their corresponding power-waveform factor (k_p) and current-waveform factor (k_i) [18]. The peak value of phase-air-gap EMF for AFPM motor in Equation (13) is:

$$E_{pk} = K_e N_{ph} B_g \frac{f_e}{p}(1-\lambda^2)D_o^2 \tag{16}$$

K_e is EMF factor, incorporating winding distribution factor (k_w) and per-unit portion of air-gap area (total) spanned by machine's salient poles (if any); N_{ph} is the number of winding turns per phase; B_g is the air-gap flux density; f_e isthe converter frequency; P is the machine pole pairs. Equation (13)'s peak phase current is:

$$I_{pk} = A\pi\, k_i \frac{1+\lambda}{2}\frac{D_o}{2m_1 N_{ph}} \tag{17}$$

where m_1 is the number of phases of each stator, and A is electrical loading. A general-purpose sizing equation for AFPM machines takes the following form:

$$P_{out} = \frac{1}{1+k_\varphi}\frac{m}{m_1}\frac{\pi}{2}k_e k_i k_p k_L \eta B_g A \frac{f_e}{P}(1-\lambda^2)\frac{1+\lambda}{2}D_o^2\, L_e \tag{18}$$

L_e is the motor's effective axial length; k_φ is the electrical loading ratio of the rotor and the stator; k_L is the aspect ratio coefficient pertinent to a specific machine structure, with considerations for the effects of losses, temperature rise, and the design's efficiency requirements. Machine torque density for the total volume is defined as:

$$\tau_{den} = \frac{P_{out}}{\omega_m \frac{\pi}{4} D_{tot}^2\, L_{tot}} \tag{19}$$

Table 3. Typical prototype waveforms.

Model	$e\ (t)$	$i\ (t)$	k_i	k_p
Sinusoidal	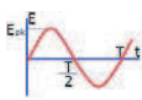	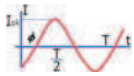	$\sqrt{2}$	$0.5\text{Cos}\varphi$
Sinusoidal	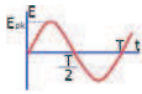	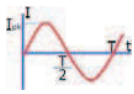	$\sqrt{2}$	0.5
Rectangular	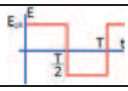	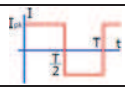	1	1
Trapezoidal	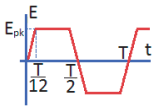	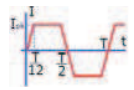	1.134	0.777
Triangular	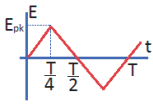	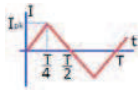	$\sqrt{3}$	0.333

ω_m is rotor angular speed, D_{tot} and L_{tot}, respectively, are the total of the machine's outer diameter and total of the machine's length including stack outer diameter and end-winding protrusion from radial and axial iron stacks.

The generalized sizing equation approach can easily be applied to double-sided AFPM TORUS-type motor. The outer surface diameter (D_o) can be written as:

$$D_o = \sqrt[3]{\frac{P_{out}}{\frac{\pi m}{2m_1} k_e k_p k_i A B_g \eta \frac{f_e}{p} (1-\lambda^2)(\frac{1+\lambda}{2})}} \tag{20}$$

The machine outer diameter total D_{tot} for the TORUS motor is given by:

$$D_{tot} = D_o + 2W_{cu} \tag{21}$$

where W_{cu} is protrusion of the end winding from the iron stack, in radial direction. For back-to-back wrapped winding, protrusions exist towards the machine axis as well as towards the outsides, and can be calculated as:

$$W_{cu} = \frac{D_i - \sqrt{D_i^2 - \frac{2AD_{ave}}{k_{cu}J_s}}}{2} \tag{22}$$

where D_{ave} is the average diameter of the machine, J_s is the slot current density, and k_{cu} is the copper fill factor. Axial length L_e of the machine is given by:

$$L_e = L_s + 2L_r + 2g \tag{23}$$

L_r is the rotor's axial length, and g is the air-gap length. Axial length of the stator L_s can be written as:

$$L_s = L_{cs} + 2L_{ss} \tag{24}$$

Note that for slotted machines, depth of the stator slot is $L_{ss} = W_{cu}$. Axial length of stator core L_{cs} can be written as:

$$L_{cs} = \frac{B_g \pi \alpha_p D_o (1+\lambda)}{4pB_{cs}} \tag{25}$$

where B_{cs} is the flux density in the stator core, and α_p is the ratio of the average air-gap flux density to the peak air-gap flux density. Axial length of the rotor, L_r, becomes:

$$L_r = L_{cr} + L_{pm} \tag{26}$$

L_{pm} is the permanent-magnet length; axial length of the rotor core, L_{cr}, is:

$$L_{cr} = \frac{B_u \pi D_o (1+\lambda)}{8pB_{cr}} \tag{27}$$

where B_{cr} is flux density in the rotor disc core, and B_u is the flux density attainable on the permanent-magnet surface. Permanent-magnet length L_{pm} can be calculated as:

$$L_{pm} = \frac{\mu_r B_g}{B_r - \left(\frac{k_f}{k_d} B_g\right)} k_C g \tag{28}$$

where μ_r is the magnet's recoil relative permeability, B_r is the permanent-magnetmaterial-residual-flux density, k_d is the leakage flux factor, k_C is Carter factor, $k_f = B_{gpk}/B_g$ is the peak value corrected factor of the air-gap flux density in radial direction of the AFPM motor. These factors can be obtained from FEM analysis [20].

4. SIMULATION RESULTS AND DISCUSSION

3D-FEA analyzed the magnetic circuit and power density of the double-sided slotted TORUS AFPM motor, for an overall picture of the saturation levels in various parts of the motor, and to extract the motor's characteristics. An advantage of 3D-FEA is that various components of flux density can be calculated highly accurately [23, 24]. Note that FEM (Finite Element Method) facilitates field analysis of

electromagnetic problems with complex geometries [25–28]. The design was simulated on commercial Vector Field Opera 14.0 3D software [29]. Corresponding materials and circuit currents were assigned to each block of the model.The simulation model reached the output (10 kW) targeted for EV. The motor's 3D model is symmetric, so 6 magnetic poles were sliced to reduce simulation/calculation time, and the model became one magnetic pole piece.For simulation, input parameters to be considered were permanent-magnet thickness, air-gap width, and magnetic properties of all the active materials. Table 4 lists the motor's design dimensions and specifications.

Table 4. The motor's final design dimensions and specifications.

Rated Voltage (*Line-Line RMS*)	V_{nom}	130 V
Rated Power	P_{nom}	10 kW
Number of pole pairs	P	3
Number of phases	m	3
Drive Frequency	f	50
Efficiency	η	91.5%
Outer Diameter	D_o	240 mm
Inner Diameter	D_i	139 mm
Inner to Outer Diameter's Ratio	λ	0.58
Magnet's axial length	L_{pm}	12 mm
Pole Pitch	γ_p	117°
Permanent magnet Skew	θ_i	7°
Stator-yoke thickness	$2 \times L_{cs}$	41 mm
Rotor-yoke thickness	L_{cr}	9 mm
Slot Bottom Width	W_{sb}	6
Slot Top Width	W_s	3
Slot Depth	D_s	11 mm
Slot Top Depth 1	d_1	3
Slot Top Depth 2	d_2	3
Number of slots	N_s	18
Number of winding turns per phase	N_{ph}	$(18 \times 10)/3$
Air-Gap Flux Density	B_g	0.71 T
Air-gap length	g	2 mm

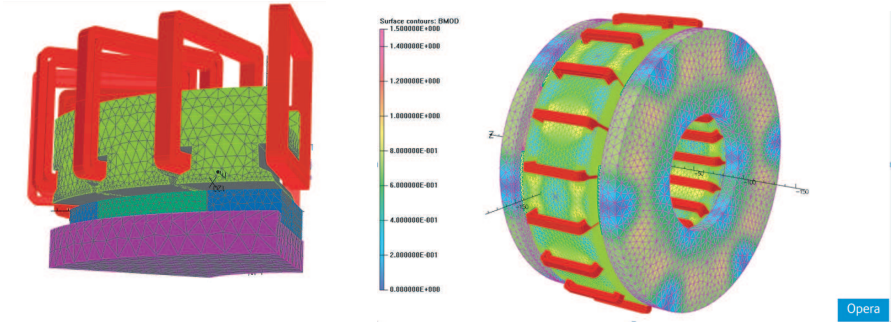

(a) (b)

Figure 4. Field analysis of an AFPM machine, in vector field opera 14.0 software. (a) 3D auto-mesh generation. (b) Flux-density plot.

Figure 4 shows only one twelfth of the motor modeling the structure of the FEA-designed AFPM: 60 degrees of the entire motor structure and 1 pole, fulfilling symmetry conditions. The whole machine comprises 18 slots and 3 pole-pairs. Fig. 4(a) (generated on Vector Field Opera 14.0 software) is a 3D auto-mesh: tetrahedral elements with 6 nodes fitting circular shape of the layers starting from inner to outer diameter of the AFPM machine [29]. Fig. 4(b) is the distribution of the magnetic flux density in various sectors of the AFPM machine. Appendix A presents the optimized winding configuration for various numbers of slots of the brushless DC AFPM motor.The best winding configuration (for 18 slots) was used here, giving as sinusoidal waveform as possible (see Fig. A1(d)). Magnetic flux density evaluation in the various sectors of an AFPM machine is important because if the flux density of the core or the teeth goes to saturation, machine efficiency reduces, affecting operation. Fig. 5 is the air-gap flux density distribution, in average radius. The maximum flux density is obviously 0.95 Tesla, averaging 0.71 Tesla.

Figure 6 shows the magnetic flux density in stator yoke and teeth at average radius. The maximum magnetic flux was 0.95 Tesla, averaging 0.67 Tesla. The flux density in the stator teeth reaches 1.5 Tesla, which, based on material limits, is the maximum allowable value. Fig. 7 is the magnetic flux density distribution in average radius for rotor yoke and magnet surface. Figs. 5, 6, and 7 give the flux density distribution, all in average radius, in Tesla. The presentation enables comparison of the simulation results from FEA with those obtained from the sizing equation. Table 5 lists the average magnetic flux density compared between FEA simulation results and sizing equation analysis,

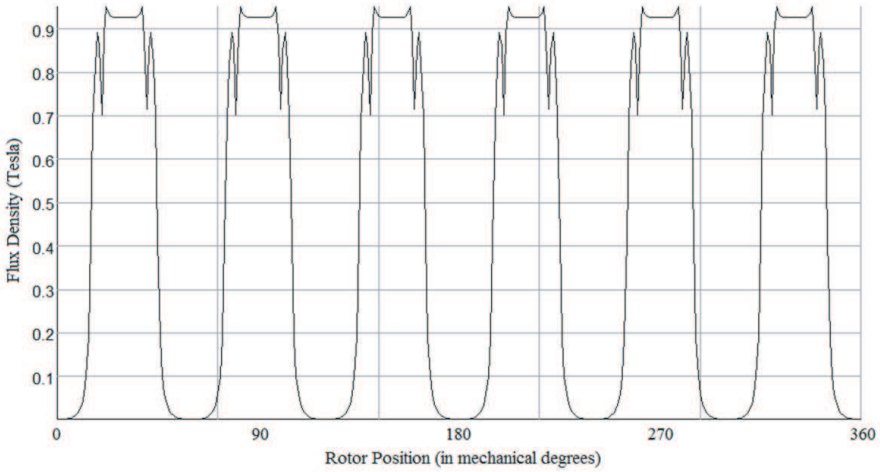

Figure 5. Magnetic flux density distribution of air-gap, for average radius.

Table 5. Magnetic flux density compared among various parts of the motor, at no-load condition.

	Air-gap		Stator yoke		Rotor yoke		Magnet surface	
	B_g		B_{cs}		B_{cr}		B_m	
	Ave.	*Max.*	*Ave.*	*Max.*	*Ave.*	*Max.*	*Ave.*	*Max.*
FEA	*0.71*	*0.95*	*0.67*	*0.95*	*0.82*	*1.15*	*0.97*	*1.10*
Sizing Eq.	*0.70*	*0.95*	*0.64*	*0.95*	*0.80*	*1.10*	*0.96*	*1.10*

at no-load condition, for various parts of the motor design. The flux density obtained from FEA was a little less than that calculated theoretically via the sizing equation, owing to core magnetic reluctance having been neglected. In real conditions, however, flux density of the different core parts decreases via MMF drop.

The slotted-TORUS configuration used in this paper is north-north magnet arrangement. The phase winding is wound around the stator core, giving a short end-winding. It reduces copper losses, but the main flux has to flow circumferentially along the stator core. Figs. 8 and 9 respectively show the magnetic flux path in the stator teeth and the magnetic potential vectors for the rotor magnets, modeled in Vector Field Opera-3D 14.

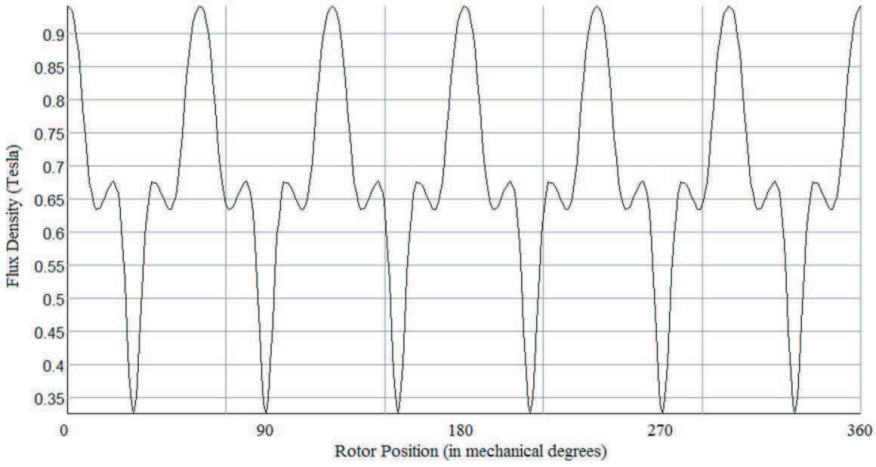

(a)

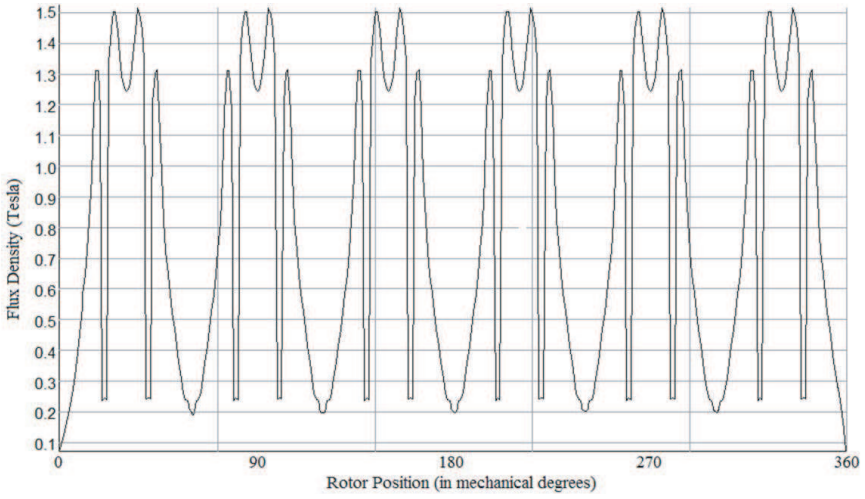

(b)

Figure 6. Stator magnetic flux density, for average radius. (a) Stator yoke. (b) Stator teeth.

4.1. Back-EMF Waveform

One well-known approach to minimizing cogging torque is magnet skewing. It also reduces back-EMF total harmonic distortion (THD) and eliminates some of the undesired harmonic components. The

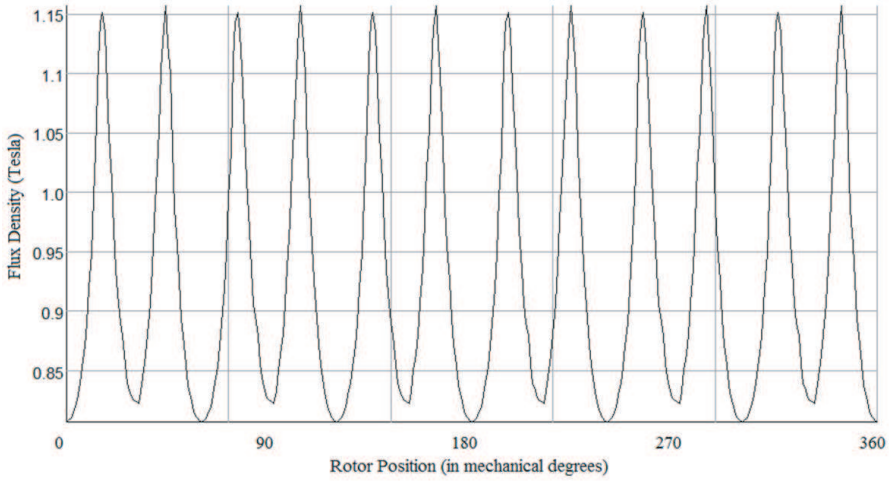

(a)

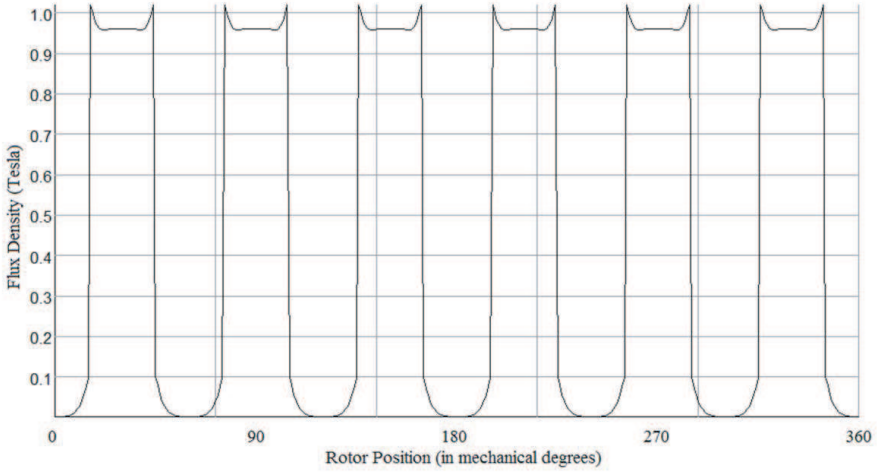

(b)

Figure 7. Magnetic flux density distribution for average radius, on (a) rotor yoke; (b) magnet surface.

maximum magnet skewing angle relative to the stator teeth should be equal to the slot pitch, not exceed it. Fig. 10(a) shows magnet's geometric skewing relative to stator teeth. Fig. 10(b) shows the back-EMF THD variation versus magnet skewing angle θ_i. The aim is to design an AFPM machine that hasa sinusoidal waveform(the back

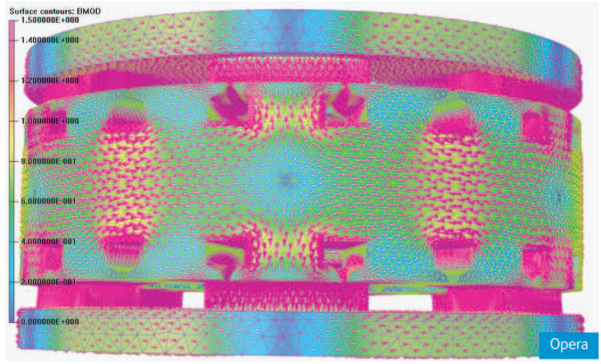

Figure 8. Flux path in stator yoke and teeth of slotted-TORUS AFPM motor.

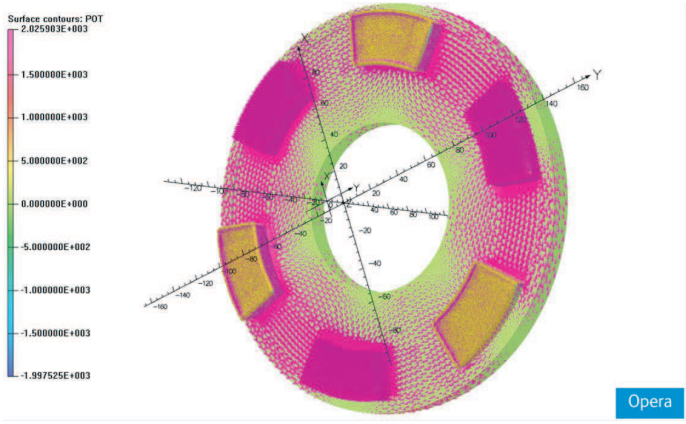

Figure 9. Magnetic potential vectors for rotor and permanent magnets.

EMF should be as sinusoidal as possible). The minimum THD occurs when the magnet skewing angle is 7 degrees. Fig. 11 shows the back EMF at 1000 rpm rated speed, also the FEA-calculated THD and back-EMF RMS.The Fourier transform of the back-EMF waveform is obtained as indicated in Fig. 12. THD significantly decreased from 26.7% to 3.1% after a 7-degree optimized magnet-skewing.

4.2. Torque

In torque performance assessment, both torque density and torque ripple must be considered. Asdo RFPM machines, AFPM machines,

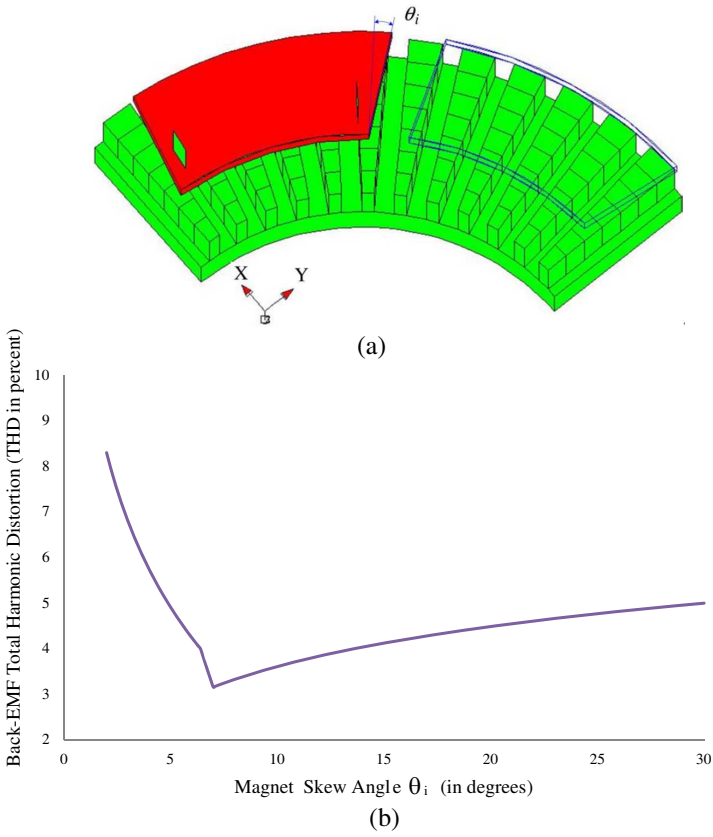

Figure 10. Permanent magnet skewing. (a) A diagram of magnet's geometric skewing relative to stator teeth. (b) THD variation versus permanent magnet skewing angle θ_i.

too, produce undesirable performance-affecting torque ripples. Main sources of torque ripple are: cogging torque, non-ideal back EMF waveforms, and saturation of machine's magnetic circuit. In designing a motor, undesired harmonics that make back EMF non-ideal are reduced by creating a back-EMF waveform that is as sinusoidal as possible. Saturation of the proposed machine's magnetic circuit in various motor parts was controlled by FEA simulation of its electromagnetic field. Cogging torque is also an issue in machine design. It results from permanent magnet's tendency to align itself at the position of minimum magnetic reluctance path between rotor and stator. Permeance variation in the slot opening leading tangential forces in the rotor, owing to flux entering the teeth, creates an

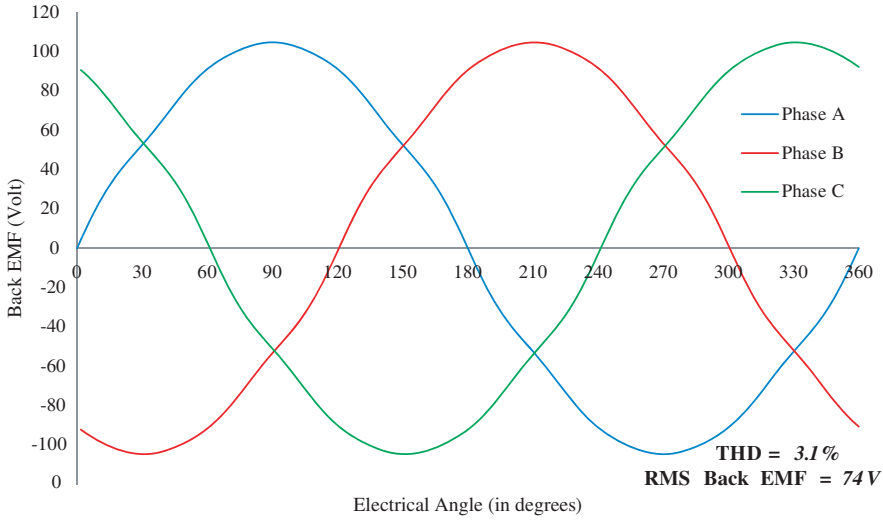

Figure 11. Back EMF at speed 1000 rpm.

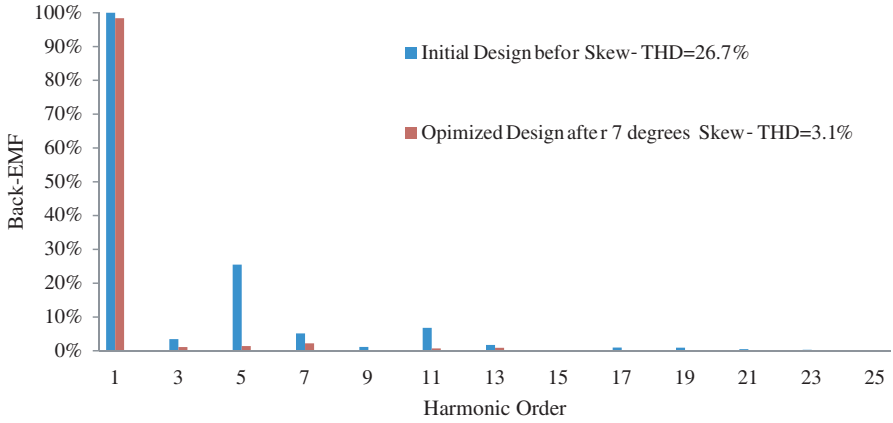

Figure 12. Comparison of harmonic components for initial and optimized design.

oscillatory output called cogging torque,which introduces noise and vibration, both of which degrade the response of high-performance motion control particularly at low speed and light loads.

An effective, most simple and common technique to reduce cogging torque is skewing. It is done by either stator slots or rotor permanent magnet skewing. Since stator slot skewing is relatively difficult to

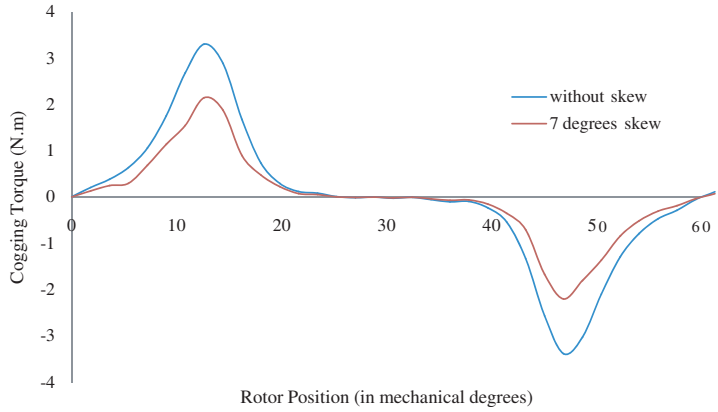

Figure 13. Cogging torque versus mechanical angle.

achieve in AFPM machines, the magnets instead are skewed. Fig. 13 shows the cogging torque of the AFPM machine, with, and without, permanent magnet skewing. Pre-skewing peak cogging torque was 3.3 Nm. Skewed magnets reduce cogging torque; at 7-degree skewing, peak cogging torque reduced to 2.1 Nm (a 36% reduction).

4.3. Efficiency

For accurate assessment of machine efficiency and thermal behavior,calculation of the losses is crucial. Machine efficiency is:

$$\eta = \frac{P_{out}}{P_{out} + P_{cu} + P_{cor} + P_{rot}} \tag{29}$$

where P_{cu}, P_{cor}, P_{rot} are respectively copper losses, core losses, and rotational losses. Copper loss ($R_s \times I^2$) makes up most of the loss total. Stator resistance (R_s) depends on load and on winding temperature [30].

$$R_s = \frac{2\, N_{ph\text{-}s}\, (l + l_e)}{\sigma_T N_{ph\text{-}p}\, s_{cu}} \tag{30}$$

$N_{ph\text{-}s}$ is the number of winding turns in series per phase, $N_{ph\text{-}p}$ is the number of winding turns in parallel per phase, σ_T is electric conductivity of wire at temperature T, and s_{cu} is cross-sectional area of wire. Thin parallel wires minimized skin effect, eliminating its consideration in Equation (30). l and l_e respectively are coil length and end-winding length.

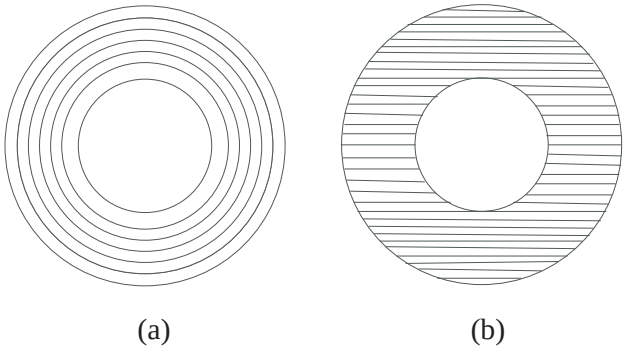

Figure 14. Spiral and axial lamination of an axial-flux motor's stator. (a) Spiral lamination. (b) Axial lamination.

Hysteresis loss (P_h) and eddy current loss (P_e) make up the motor core loss and can be calculated from:

$$P_h = \frac{k_h \cdot B_m^n \cdot f^2}{\rho} \tag{31}$$

$$P_e = \frac{k_e \cdot B_m^2 \cdot f^2}{\rho} \tag{32}$$

k_h, k_e, $B_{\max}$, and ρ respectively are hysteresis constant, eddy current constant, maximum flux density, and core material density. FE-AC analysis was repeated for every space harmonic component (up to the 49th order) and for every current waveform's simulated time harmonic component, to get the eddy current losses in the stator steel. The stator of an axial-flux motor is laminated either spirally or axially (see Fig. 14 for their configurations). Each made from silicon steel, the thickness of the laminating silicon steel paper is 0.1 mm. In this work, spiral lamination was used in the simulations. The core loss for the stator laminated 0.1 mm thick, calculated via FE-AC analysis, was 63 W.

Figure 15 shows the motor's efficiency in various speeds. Rotational loss (which includes windage and friction losses) was estimated from the following Equation [31]:

$$P_{rot} = \frac{1}{2} c_f \rho_r \left(\pi\, n^3\right) \left(D_o^5 - D_i^5\right) \tag{33}$$

where c_f is friction coefficient, ρ_r is density of the rotating part, and n is rotation speed (in 'rotation per second'). Efficiency of the laminated-stator motor, obtained with full loading at full load, was 91.5 %.

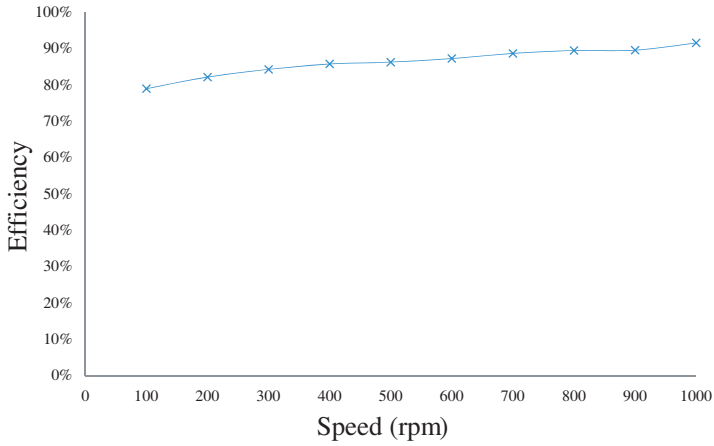

Figure 15. Efficiency versus speed.

5. CONCLUSION

The design and simulation of a slotted TORUS AFPM motor for EV application has been presented. The motor produced 10 kW power and the maximum amplitude of the sinusoidal back EMF was 105 V at 1000 rpm rated speed. Its design met specifications and requirements of EV direct drive. The requirements had been determined through a simple model of vehicle dynamics that considered a cruising scenario. Limits to material and application were considered as well. The motor's performance was increased by optimizing the design parameters (air-gap length, permanent-magnet size and material, magnet orientation, and winding configuration) via sizing equation and Finite Element Analysis. The simulated and desired values agreed. Comparison of FEA and sizing equation shows the design's flux density at no-load condition and in various parts of the motor agreeing. The design process is comprehensive and can be used for an arbitrary EV considering an arbitrary cruising scenario.

APPENDIX A. WINDING CONFIGURATIONS

A method described in [32] was used to place the coils. There are infinite possibilities for pole and slot-count combinations as there are for winding layouts; assumptions are necessary, either for focus or for scope limitation, so desirable windings can be found. The assumptions were:

a) Three-phase motor.

b) All slots filled; the number of slots is thus a multiple of the number of phases (i.e., $N_s = k \times N_{ph}$); for three-phase motors, the number of slots is thus always a multiple of three.

c) Two coil-sides in each slot, the winding can be classified as double-layer winding.

d) Balanced-windings only, i.e., only pole and slot-count combinations that result in back EMF of phases B and C being $120^{\circ E}$ offset from back EMF of phase A.

e) Coils have equal number of turns, all spanning equal number of slots, implying same-sized coils and therefore same resistance and same inductance.

The assumptions routinely lead to motors capable of high performance, and to motors that are readily wound. Motors can be wound violating one or more of the assumptions, but they may be more difficult to wind; such winding could also lower performance. Fig. A1 shows the coil arrangements (9, 12, 15, 18, 21, and 24 slots) that gave the best sinusoidal waveforms. A, B, and C represent the phases, and + and − represent direction of the windings.

The number of winding configuration options can also be increased by short-pitching the fractional-slot structures. The 15-slot stator was

Table A1. Possible winding configurations and number of slots in each pole, per phase.

Configuration Number	Number of Slots	Coil Pitch/Pole Pitch	Number of slots in each pole per phase (N_{spp})
1	9	2/2.25	0.75
2	12	2/3	1
3	12	full-pitch	1
4	15	2/3.75	1.25
5	15	3/3.75	1.25
6	18	3/4.5	1.5
7	18	4/4.5	1.5
8	21	3/5.25	1.75
9	21	4/5.25	1.75
10	21	5/5.25	1.75
11	24	4/6	2
12	24	5/6	2
13	24	full-pitch	2

Slot No.	1	2	3	4	5	6	7	8	9
up	+A	-B	-A	+B	-C	-B	+C	-A	-C
down	+A	+C	-A	+B	+A	-B	+C	+B	-C

(a)

Slot No.	1	2	3	4	5	6	7	8	9	10	11	12
up	+A	-B	+C	-A	+B	-C	+A	-B	+C	-A	+B	-C
down	+A	-B	+C	-A	+B	-C	+A	-B	+C	-A	+B	-C

(b)

Slot No.	1	2	3	4	5	6	7	8	9	10	11	12	13	14	15
up	+A	-B	+C	-A	+B	+B	-C	+A	+A	-B	+C	-A	+B	-C	-C
down	-B	-B	+C	+C	-A	-C	-C	+A	-B	+C	-A	-A	+B	+B	+A

(c)

Slot No.	1	2	3	4	5	6	7	8	9	10	11	12	13	14	15	16	17	18
up	+A	-B	-B	+C	-A	+B	+B	-C	+A	+A	-B	+C	+C	-A	-A	+B	-C	-C
down	+A	-B	+C	+C	-A	-A	+B	-C	-C	+A	-B	+C	+C	-A	+B	+B	-C	+A

(d)

Slot No.	1	2	3	4	5	6	7	8	9	10	11	12	13	14	15	16	17	18	19	20	21
up	+A	-B	-B	+C	+C	-A	-A	+B	-C	-C	+A	+A	-B	-B	+C	-A	-A	+B	+B	-C	-C
down	+A	-B	-B	+C	+C	-A	+B	+B	-C	-C	+A	+A	-B	+C	+C	-A	-A	+B	+B	-C	+A

(e)

Slot No.	1	2	3	4	5	6	7	8	9	10	11	12	13	14	15	16	17	18	19	20	21	22	23	24
up	+A	+A	-B	-B	+C	+C	-A	-A	+B	+B	-C	-C	+A	+A	-B	-B	+C	+C	-A	-A	+B	+B	-C	-C
down	+A	+A	-B	-B	+C	+C	-A	-A	+B	+B	-C	-C	+A	+A	-B	-B	+C	+C	-A	-A	+B	+B	-C	-C

(f)

Figure A1. Stator winding constructions for 9, 12, 15, 18, 21, and 24 slots. (a) 9-slot double-layer stator winding (coil span = 2). (b) 12-slot double-layer stator winding (full-pitch). (c) 15-slot double-layer stator winding (coil span = 2). (d) 18-slot double-layer stator winding (coil span = 4). (e) 21-slot double-layer stator winding (coil span = 5). (f) 24-slot double-layer stator winding (full-pitch).

designed with a 3-slot coil span, but a 2-slot coil span is possible, reconfiguration for it easy. For an 18-slot structure, 3-slot coil span, and for 21-slot structure, both 3-slot and 4-slot coil spans can be considered. For the 13 stator configurations in Table A1 and their possible magnet spans, their losses, back-EMF harmonic content, and pulsating torque components were investigated.Efficiencies were found to not differ much except at lower speeds, where the differences were more pronounced (owing to copper losses). The worst structure in terms of copper losses was found to be 24-slot, full-pitched.

APPENDIX B. NOMENCLATURE

A	electrical loading total [A]
A_{lin}	linear current density of the machine's inner radius [A/m]
B	magnetic flux density [T]
B_{cr}	rotor-disc flux density [T]
B_{cs}	stator-core flux density [T]
B_g	air-gap flux density [Wb/m^2]
B_{gpk}	peak value of air-gap flux density [Wb/m^2]
B_m	permanent magnet flux density [T]
$B_{\max}$	maximum flux density [T]
B_r	permanent-magnet residual-flux density [T]
B_u	flux density on permanent-magnet surface [T]
C_d	air-resistance coefficient
D_{ave}	machine stator average diameter [m]
D_i	machine stator inner diameter [m]
D_o	machine stator outer diameter [m]
D_s	slot depth [m]
D_{tot}	machine outer diameter total [m]
E_{pk}	peak value of phase-air-gap EMF [V]
F_{rm}	vehicle driving resistance force[N]
I_{rms}	phase current rms value [A]
I_{pk}	phase current peak value [A]
J	external current density [A/m^2]
J_s	slot current density [A/m^2]
H	magnetic field intensity [A/m]
K_e	EMF factor
$K_{n\times n}$	stiffness matrix
L_{cr}	rotor-core axial length [m]
L_{cs}	stator-core axial length [m]
L_e	effective axial length of motor [m]
L_{pm}	permanent-magnet length [m]
L_r	rotor axial length [m]

L_s	stator axial length [m]
L_{ss}	stator slot depth [m]
L_{tot}	machine axial length total [m]
M	vehicle mass [kg]
N_{ph}	number of winding turns per phase
N_{ph-s}	number of winding turns in series per phase
N_{ph-p}	number of winding turns in parallel per phase
N_s	number of slots [m]
P	number of motor pole pairs
P_{accel}	power required to accelerate [W]
P_{cor}	core losses [W]
P_{cu}	Copper losses [W]
P_{rot}	rotational losses [W]
P_{nom}	nominal power [kW]
$P_{\min}$	minimum required power [W]
P_{out}	rated power [W]
R_s	stator resistance [Ω]
S	frontal projected area [m^2]
S_g	air-gap area [m^2]
S_{pm}	permanent magnet area [m^2]
T	period of one EMF cycle [Sec]
V_{nom}	nominal voltage (line to line RMS) [V]
W_{cu}	end-winding protrusion from iron stack [m]
W_s	Slot opening width
W_{sb}	Slot bottom width [m]
a	vehicle acceleration [m/s^2]
a_g	gravity acceleration [m/s^2]
c_f	friction coefficient
d_1	slot top depth 1 [m]
d_2	slot top depth 2 [m]
$e(t)$	phase-air-gap EMF [V]
$i(t)$	phase current [A]

f_e	electrical frequency [Hz]
$f_e(\mathrm{t})$	normalized EMF waveforms
$f_i(\mathrm{t})$	normalized current waveforms
f_l	aerodynamic-resistance force [N]
f_r	rolling-resistance coefficient
f_{ro}	rolling-resistance force [N]
f_{st}	climbing-resistance force [N]
g	air-gap length [m]
$g_{n\times 1}$	excitation vector
k_C	Carter coefficient
k_L	aspect ratio coefficient
k_{cu}	copper fill factor
k_d	leakage-flux factor
k_e	eddy current constant
k_h	hysteresis constant
k_i	current waveform factor
k_p	electrical power waveform factor
k_f	peak value corrected factor of air-gap flux density
k_w	winding distribution factor
$k_{\sigma PM}$	a factor that takes into account the leakage flux
k_φ	electrical loading ratio
l	coil length [m]
l_e	end winding length [m]
m	number of phases
m_1	number of phases of each stator
n	rotation speed [rs^{-1}]
r	position vector [m]
s_{cu}	cross-section area of wire
t	average slot pitch [m]
v	vehicle speed [m/s]
v_0	headwind speed [m/s]
Φ	winding flux linkage [Wb]
Ψ	magnetic vector potential [$\mathrm{V}\cdot\mathrm{s}\cdot\mathrm{m}^{-1}$]
α	vehicle movement angle [Rad]

α_p	average air-gap flux density to its peak value ratio
γ	air-gap fictions coefficient
γ_p	pole pitch [in degrees]
η	motor efficiency
θ_i	Permanent magnet skew [in degrees]
λ	diameter ratio
μ	permeability [$A \cdot m^2$]
μ_0	Permeability of free space [$A \cdot m^2$]
μ_r	Relative permeability
μ_{ra}	relative permeability of the permanent magnet
ρ	core material density [kg/m^3]
ρ_a	air density [kg/m^3]
ρ_r	density of the rotating part of the motor [kg/m^3]
σ	electrical conductivity [$\Omega \cdot m$]
σ_T	electric conductivity of wire [Sm^{-1}]
τ_{den}	torque density [$N \cdot m/cm^3$]
τ_{min}	minimum required torque [$N \cdot m$]
ω_m	angular speed [Rad/s]

ACKNOWLEDGMENT

The authors acknowledge University of Malaya's provision of the High Impact Research Grant No. D000022-16001 funding the Hybrid Solar Energy Research Suitable for Rural Electrification.

REFERENCES

1. Rahim, N. A., W. P. Hew, and A. Mahmoudi, "Axial-flux permanent-magnet brushless dc traction motor for direct drive of electric vehicle," *International Review of Electrical Engineering*, Vol. 6, No. 2, 760–769, April 2011.
2. Johansen, P. R., D. Patterson, C. O'Keefe, and J. Swenson, "The use of an axial flux permanent magnet in-wheel direct drive in an electric vehicle," *Renewable Energy*, Vol. 22, No. 1–3, 151–157, January–March 2001.
3. Kim, M. J., B. K. Kim, J. W. Moon, Y. H. Cho, D. H. Hwang, and D. S. Kang, "A method for diagnosis of induction machine fed by PWM vector control," *International Journal of Applied*

Electromagnetics and Mechanics, Vol. 28, No. 1, 2, 275–281, September 2008.

4. Nguyen, P. H., E. Hoang, and M. Gabsi, "Performance synthesis of permanent-magnet synchronous machines during the driving cycle of a hybrid electric vehicle," *IEEE Transaction on Vehicular Technology*, Vol. 60, No. 5, 1991–1998, June 2011.
5. Dai, Y., L. Song, and S. Cui, "Development of PMSM drives of hybrid electric car applications," *IEEE Transaction on Magnetics*, Vol. 43, No. 1, 434–437, January 2007.
6. Baoquan, K., L. Chunyan, and C. Shukang, "Flux-weakening-characteristic analysis of a new permanent-magnet synchronous motor used for electric vehicles," *IEEE Transaction on Plasma Science*, Vol. 39, No. 1, 511–515, January 2011.
7. Choi, J. H., Y. D. Chun, P. W. Han, M. J. Kim, D. H. Koo, J. Lee, and J. S. Chun, "Design of high power permanent magnet motor with segment rectangular copper wire and closed slot opening on electric vehicles," *IEEE Transaction on Magnetics*, Vol. 46, No. 6, 2070–2073, June 2010.
8. Yang, Y. P., Y. P. Lah, and C. H. Cheung, "Design and control of axial-flux brushless DC wheel motors for electric vehicles-part I: Multiobjective optimal design and analysis," *IEEE Transaction on Magnetics*, Vol. 40, No. 4, 1873–1882, July 2004.
9. Yang, Y. P., Y. P. Lah, and C. H. Cheung, "Design and control of axial-flux brushless DC wheel motors for electric vehicles-part II: Optimal current waveforms and performance test," *IEEE Transaction on Magnetics*, Vol. 40, No. 4, 1883–1891, July 2004.
10. Rahman, K. M., N. R. Patel, T. G. Ward, J. M. Nagashima, F. Caricchi, and F. Crescimbini, "Application of direct-drive wheel motor for fuel cell electric and hybrid electric vehicle propulsion system," *IEEE Transaction on Industry Applications*, Vol. 42, No. 5, 1185–1192, September–October 2006.
11. Cavagnino, A., M. Lazzari, F. Profumo, and A. Tenconi, "A comparison between the axial flux and the radial flux structures for PM synchronous motors," *IEEE Transaction on Industrial Applications*, Vol. 38, No. 6, 1517–1524, November–December 2002.
12. Mahmoudi, A., N. A. Rahim, and W. P. Hew, "Axial-flux permanent-magnet machine modeling, design, simulation, and analysis," *Scientific Research and Essay*, Vol. 6, No. 12, 2525–2549, June 2011.
13. Mahmoudi, A., N. A. Rahim, and W. P. Hew, "Analytical method for determining axial-flux permanent-magnet machine

sensitivity to design variables," *International Review of Electrical Engineering*, Vol. 5, No. 5, 2039–2048, September–October 2010.

14. Mahmoudi, A., N. A. Rahim, and W. P. Hew, "An analytical complementary FEA tool for optimizing of axial-flux permanent-magnet machines," *International Journal of Applied Electromagnetics Machines*, Vol. 37, No. 1, 19–34, September 2011.
15. Gieras, J. F., R. J. Wang, and M. J. Kamper, *Axial Flux Permanent Magnet Brushless Machines*, Springer Verla, 2008.
16. Mahmoudi, A., N. A. Rahim, and W. P. Hew, "TORUS and AFIR axial-flux permanent-magnet machines: A comparison via finite element analysis," *International Review on Modelling and Simulations*, Vol. 4, No. 2, 624–631, April 2011.
17. Gholamian, S. A., "Optimum design and manufacturing of axial flux permanent magnet motor for electric vehicle application," Ph.D. Dissertation, K. N. Toosi Univ. Technology, Tehran, Iran, January 2008.
18. Huang, S., J. Luo, F. Leonardi, and T. A. Lipo, "A general approach to sizing and power density equations for comparison of electrical machines," *IEEE Transaction on Industry Applications*, Vol. 34, No. 1, 92–97, January–February 1998.
19. Huang, S., J. Luo, F. Leonardi, and T. A. Lipo, "A comparison of power density for axial flux machines based on the general purpose sizing equation," *IEEE Transaction on Energy Conversion*, Vol. 14, No. 2, 185–192, January 1999.
20. Aydin, M., S. Huang, and T. A. Lipo, "Design and 3D electromagnetic field analysis of non-slotted and slotted TORUS type axial flux surface mounted permanent magnet disc machines," *IEEE International Electric Machines and Drives Conference*, January 17th–20th, 2001.
21. Aydin, M., S. Huang, and T. A. Lipo, "Optimum design and 3D finite element analysis of nonslotted and slotted internal rotor type axial flux pm disc machines," *IEEE Power Engineering Society Summer Meeting*, July 15th–19th, 2001.
22. Mahmoudi, A., N. A. Rahim, and H. W. Ping, "Genetic algorithm and finite element analysis for optimum design of slotted Torus axial-flux permanent-magnet brushless DC motor," *Progress In Electromagnetics Research B*, Vol. 33, 383–407, 2011.
23. Liu, C. T. and S. C. Lee, "Magnetic field modeling and optimal operational control of a single-side axial-flux permanent magnet motor with center poles," *Journal of Magnetism and Magnetic Materials*, Vol. 304, No. 1, 454–456, September 2006.

24. Liu, C. T., S. C. Lin, and T. S. Chiang, "On the analytical flux distribution modeling of an axial-flux surface-mounted permanent magnet motor for control applications," *Journal of Magnetism and Magnetic Materials*, Vol. 282, 346–350, November 2004.
25. Vaseghi, B., N. Takorabet, and F. Meibody-Tabar, "Transient finite element analysis of induction machines with stator winding turn fault," *Progress In Electromagnetics Research*, Vol. 95, 1–18, 2009.
26. Torkaman, H. and E. Afjei, "FEM analysis of angular misalignment fault in SRM magnetostatic characteristics," *Progress In Electromagnetics Research*, Vol. 104, 31–48, 2010.
27. Torkaman, H. and E. Afjei, "Comparison of two types of dual layer generator in field assisted mode utilizing 3D-FEM and experimental verification," *Progress In Electromagnetics Research B*, Vol. 23, 293–309, 2010.
28. Torkaman, H. and E. Afjei, "Magnetio static field analysis regarding the effects of dynamic eccentricity in switched reluctance motor," *Progress In Electromagnetics Research M*, Vol. 8, 163–180, 2009.
29. Opera Version 14.0 User Guide, Vector Fields, 2011, http://www.cobham.com.
30. Wang, R. J., M. J. Kamper, and K. V. D. Westhuizen, "Optimal design of a coreless stator axial flux permanent magnet generator," *IEEE Transaction on Magnetics*, Vol. 41, No. 1, 55–64, January 2005.
31. Saari, J., "Thermal analysis of high-speed induction machines," Ph.D. Dissertation, Helsinki Univ. Technology, Helsinki, Finland, January 1998.
32. Hanselman, D. C., *Brushless Permanent Magnet Motor Design*, McGraw-Hill, New York, 1994.